Desalination and Water Treatment
www.deswater.com

doi:10.5004/dwt.2019.23659

145 (2019) 318–325
March

Co_3O_4-ZrO_2 nanocomposites: simple preparation and enhanced photocatalytic performance for cyanide degradation under visible light

K.S. Al-Namshah[a], R.M. Mohamed[b,c,*]

[a]*College of Science, Main Campus King Abdullah Rd, King Khalid University, Abha, Saudi Arabia, email: redama123@yahoo.com (K.S. Al-Namshah)*
[b]*Department of Chemistry, Faculty of Science, King Abdulaziz University, PO Box 80203, Jeddah 21589, Saudi Arabia,(R.M. Mohamed)*
[c]*Advanced Materials Department, Central Metallurgical R&D Institute, CMRDI, P.O. Box 87 Helwan, Cairo, Egypt*

Received 27 June 2018; Accepted 23 December 2018

ABSTRACT

Zirconium dioxide (ZrO_2) has a wide band gap and fast electron-hole recombination rate. Therefore, the photocatalytic activity of ZrO_2 is very small, and it absorbs ultraviolet region. Thus, the separation of electrons and holes can enhance the photocatalytic activity of ZrO_2. Here, Co_3O_4-ZrO_2 nanocomposites were synthesized using a sol-gel route utilizing cetyl trimethylammonium bromide as a template. The degradation of cyanide was used as a control test to evaluate the performance of the photocatalytic activity of the Co_3O_4-ZrO_2 photocatalysts. The findings demonstrate that the weight percent of cobalt oxide could be reduced the band gap energy of zirconium dioxide. The band gap of ZrO_2 was reduced from 3.42 to 2.65 eV by the addition of 3 wt% Co_3O_4. The photodegradation efficiency reached 100% within 30 min using a 3 wt% Co_3O_4-ZrO_2 photocatalyst. The 3 wt% Co_3O_4-ZrO_2 photocatalyst can be used five times with stable photocatalytic activity.

Keywords: CO_3O_4-ZrO_2; Visible light; Cyanide degradation

1. Introduction

Extremely contaminated waste containing cyanide ions is extensively produced from metal finishing units and electroplating. The occurrence of complex or free cyanide compounds in manufacturing wastewater causes serious problems for the environment and human health. Cyanide can be degraded by different techniques, such as biological, chemical [1] and physical routes[2]. In physical routes, the cyanide is transferred from one phase to another phase, as carried out in foam flotation, adsorption and ion exchange. The disadvantage of biological routes is their low efficiency; they are applicable to low cyanide concentrations. Additionally, they produce sludge, and the removal of sludge is very problematic. Cyanide can be disposed of by alkaline chlorination. However, the drawbacks for this method are the removal of toxic cyanide by more toxic cyanogen chloride gas as well as the remaining metal cyanide complex in the sludge. The photocatalysis process is one efficient method for the degradation of cyanide using titanium dioxide and zinc oxide [3–8]. The drawbacks for commercial use of these photocatalysts are the fast recombination of electrons and holes, as well as their excitation by ultraviolet light. Therefore, the photocatalyst for commercial use needs to hinder the recombination of electrons and holes, as well as use solar radiation for the excitation of the photocatalysts. Many scientists have used a variety of ways to develop the photocatalysts' properties for preferred functions. One of these methods is varying the process of photocatalyst preparation [9]. The variation of bandwidth of the photocatalysts is a vital concern in photocatalyst selections. For that reason, the bandwidth of photocatalysts can be varied by different routes, such as doping the photocatalyst by different metals using many approaches to hinder the recombination of electrons and holes, as well as using solar radiation for the

---

*Corresponding author.

excitation of photocatalysts [10]. Multiple-semiconductor devices can harvest a larger solar spectrum region, which is useful for the semiconductor excitation and therefore the photoinduced generation of charge carriers. In addition, the merging of two diverse semiconductors like ZrO_2 and CO_3O_4 could move photogenerated electrons from an excited small bandgap semiconductor to the other close contact one in the case of proper conduction band potentials. This supports the photoinduced holes and electrons separation and thus promotes the photocatalytic activity of heterostructure of semiconductor materials [11].

ZrO_2 is a highly useful photocatalyst extensively applied in the petroleum industry for the deformation, isomerization, and dehydrogenation of organic compounds. Additionally, ZrO_2 has been used as a photocatalyst for the mineralization and decomposition of many pollutants. It has a wide band gap energy and its band gap depends on the formed phase. ZrO_2 has three phases, and each phase has different band gap values [12]. The band gap values of cubic, monoclinic and tetragonal zirconium dioxide are 3.25–12.30, 3.12–5.42 and 4.10–13.30 eV, respectively [13,16]. ZrO_2 was incorporated with iron, vanadium and nickel ions to improve its photocatalytic activity by reducing the band gap and hindering the recombination of electrons and holes [13,17]. Additionally, doped metals ions improve the photocatalytic activity of ZrO_2 by changing its phases and crystallite size [14–18].

The coupling of ZrO_2 with another semiconductor is another approach to improve its photocatalytic activity by reducing its band gap and hindering the recombination of electrons and holes. Co_3O_4 has a band gap energy of 2.19 eV and absorbs in the visible region [19]. The Co_3O_4-ZnO nanocomposite has a narrow band gap compared to the ZnO photocatalyst [20]. Additionally, Co_3O_4 can be combined with different semiconductors, such as TiO_2 [21]. Until the present, the Co_3O_4-ZrO_2 nanocomposite had not been studied. In this study, we investigated the preparation and photocatalytic performance of the Co_3O_4-ZrO_2 nanocomposite. The Co_3O_4-ZrO_2 photocatalytic performance was measured by studying cyanide decomposition under visible light.

2. Experimental

2.1. Photocatalysts synthesis

A total of 4 g of CTAB (Cetyl trimethylammonium bromide) was dissolved in doubly distilled water (20 mL). After that, 20 mL of isopropyl alcohol and 2 mL of nitric acid were added to the CTAB solution and stirred at room temperature for 30 min. Then, 0.5 mmol of zirconium isopropoxide was added to the above mixture and stirred at room temperature for 30 min. Lastly, cobalt isopropoxide was added, and the obtained mixture was stirred at room temperature for 30 min and left to form a gel. The amount of added cobalt isopropoxide was varied to prepare different wt% samples of Co_3O_4 to ZrO_2, such as ZrO_2, 1 wt% Co_3O_4/ZrO_2, 3 wt% Co_3O_4/ZrO_2 and 5 wt% Co_3O_4/ZrO_2. The obtained gel was dried for 24 h at 100°C. The obtained materials were calcined at 550°C for 3 h. To prepare ZrO_2, the earlier steps were repeated without using cobalt isopropoxide.

2.2. Photocatalysts characterizations

The ZrO_2 and Co_3O_4-ZrO_2 nanocomposite band gap values were determined from UV-Vis spectra, which were investigated with a UV-Vis-NIR spectrophotometer (model V-570, Jasco, Japan). During measurement, barium sulfate was used as a reference. ZrO_2 and Co_3O_4-ZrO_2 nanocomposite. X-ray diffraction patterns were measured using a Bruker axis D8 with Cu Ka radiation (λ = 1.5418 Å), 35 mA as the emission current and 40 kV as the accelerating voltage. The photoluminescence (PL) spectra of the samples were provided using a spectrophotometer (Shimadzu RF-5301PC) at 25°C with an excitation wavelength of 300 nm. Morphology and particle size were investigated using a field emission-scanning electron microscopy (FE-SEM, Quanta FEG 250, Netherlands). The FE-SEM instrument equipped with energy dispersive X-ray (EDX) facility was used to capture SEM images and to perform elemental analysis. The sample was gold coated prior to examination by FE-SEM instrument operating at 5 kV while EDX analysis was performed at 15 kV. A transmission electron microscope was conducted at 200 kV with JEOL-JEM-1230 model to investigate the morphology and particle size. The XPS spectra were obtained with a Thermo Scientific K-ALPHA spectrometer equipped with dual aluminum–magnesium anodes using MgKα radiation as the X-ray source at a power of 150 W (accelerating voltage 12 kV, current 6 mA) in a vacuum of 8.0×10^{-8} mPa. The measured samples were prepared by dropping the colloidal solution of samples, following centrifugation and re-dispersion as colloidal solution, on freshly cleaved HOPG and subsequent drying at the room temperature. The surface areas of the ZrO_2 and Co_3O_4/ZrO_2 nanocomposites were measured using a Nova 2000 series Chromatech apparatus. An electrochemical workstation (ZahnerZennium, Germany) was used to measure the transient photocurrent of the ZrO_2 and Co_3O_4/ZrO_2 nanocomposites.

2.3. Evaluation of the photocatalytic activity

The evaluation of photocatalytic activity was investigated by measuring the cyanide degradation in the presence of visible light. A horizontal cylinder annular batch reactor was used as a photocatalytic reactor for carrying out the photocatalytic reaction. A blue fluorescent lamp with a maximum energy of 150 W at 450 nm was used as the source of irradiation. To remove UV light and pass only visible light, UV cutoff filters were used. The photocatalyst dose was suspended in 300 mL of potassium cyanide (100 ppm) solution. The pH of the reaction mixture was adjusted to 10.5 using ammonia solution to avoid hydrogen cyanide gas evolution. The reaction temperature was adjusted at 25°C, and 60 min was the total reaction time. Samples from the mixture were taken at different intervals, and the cyanide concentration in them was determined using volumetric titration, according to a published method [22]. The percent of photocatalytic activity was calculated using the following equation:

$$\% \text{ photocatalytic activity} = (C_o - C)/C_o \times 100$$

where the cyanide initial concentration in solution is C_o and the cyanide concentration remaining in the solution is C.

3. Results and discussions

3.1. Characterizations of ZrO_2 and Co_3O_4-ZrO_2 nanocomposites

Fig. 1. shows the XRD patterns of the ZrO_2 and Co_3O_4-ZrO_2 nanocomposites. The results demonstrate that only the ZrO_2 phase appeared for ZrO_2 and Co_3O_4-ZrO_2 samples, which means that no peaks for cobalt or cobalt oxide appeared for the Co_3O_4-ZrO_2 samples. Additionally, we noticed that the peaks for the ZrO_2 phase were shifted to the right side by the addition of Co_3O_4 to ZrO_2. Thus, some cobalt ions were incorporated into the zirconium oxide lattice and formed cobalt-oxygen-zirconium bonds by replacing zirconium ions with cobalt ions. The peak intensity for the ZrO_2 phase decreased with the addition of Co_3O_4 to ZrO_2.

Fig. 2 shows the XPS high resolution spectra for the Co, Zr and O species of a 3 wt% Co_3O_4-ZrO_2 sample. Two binding energies of Zr3d5/2 and Zr3d3/2 at 182.7 and 186.7 eV, respectively, provide evidence for the presence of the Zr^{4+} ions in a 3 wt% Co_3O_4-ZrO_2 sample, as revealed in Fig. 2 A. A peak at 531.4 eV for O1s provides evidence of the presence of O^{2-} ions in the 3 wt% Co_3O_4-ZrO_2 sample, as shown in Fig. 2 B. Two peaks at 779.7 and 794.9 eV for $Co2p_{3/2}$ and $Co2p_{1/2}$, respectively, provide evidence of the presence of Co_3O_4 in the 3 wt% Co_3O_4-ZrO_2 sample, as shown in Fig. 2 C. Actually, Co^{2+} has assigned at ~786 eV. However, in our study of Co_3O_4, which is mixed between Co^{2+} and Co^{3+} oxidation state. The findings exhibited that the binding energy of Co^{3+} at 779.7 and 794.9 eV for $Co2p_{3/2}$ and $Co2p_{1/2}$, respectively shifts ~2 eV to a lower value as reported in previous published paper [23–25], indicating the Co^{3+}–O^- bond in Co_3O_4 is debilitated.

Fig. 3 shows SEM images of the ZrO_2, 1 wt% Co_3O_4-ZrO_2, 3 wt% Co_3O_4-ZrO_2 and 5 wt% Co_3O_4-ZrO_2 samples. The results reveal that the shape of the ZrO_2 sample is nanorods, as shown in Fig. 3A. The addition of Co_3O_4 to the ZrO_2 sample led to the formation of nanosheets of Co_3O_4 around the nanorod shape of ZrO_2, as shown in Figs. 3B–D. Additionally, we noticed that, as the weight percent of Co_3O_4 increased, the percent of nanosheets around the nanorods increased. Fig. 4 shows TEM images of the ZrO_2, 1 wt% Co_3O_4-ZrO_2, 3 wt% Co_3O_4-ZrO_2, and 5 wt% Co_3O_4-ZrO_2 samples. The results reveal that the shape of the ZrO_2 sample is nanorods, as shown in Fig. 4 A. The addition of Co_3O_4 to the ZrO_2 sample led to the formation of nanosheets of Co_3O_4 around the nanorod shape for ZrO_2, as shown in Figs. 4B–D. Additionally, we noticed that, as the weight per-

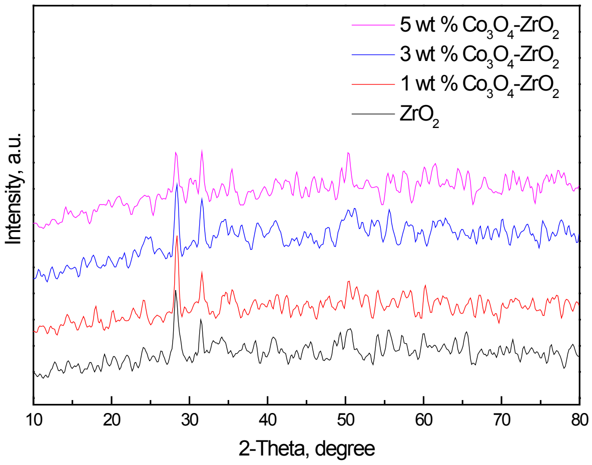

Fig. 1. XRD patterns of the ZrO_2 and Co_3O_4-ZrO_2 nanocomposites.

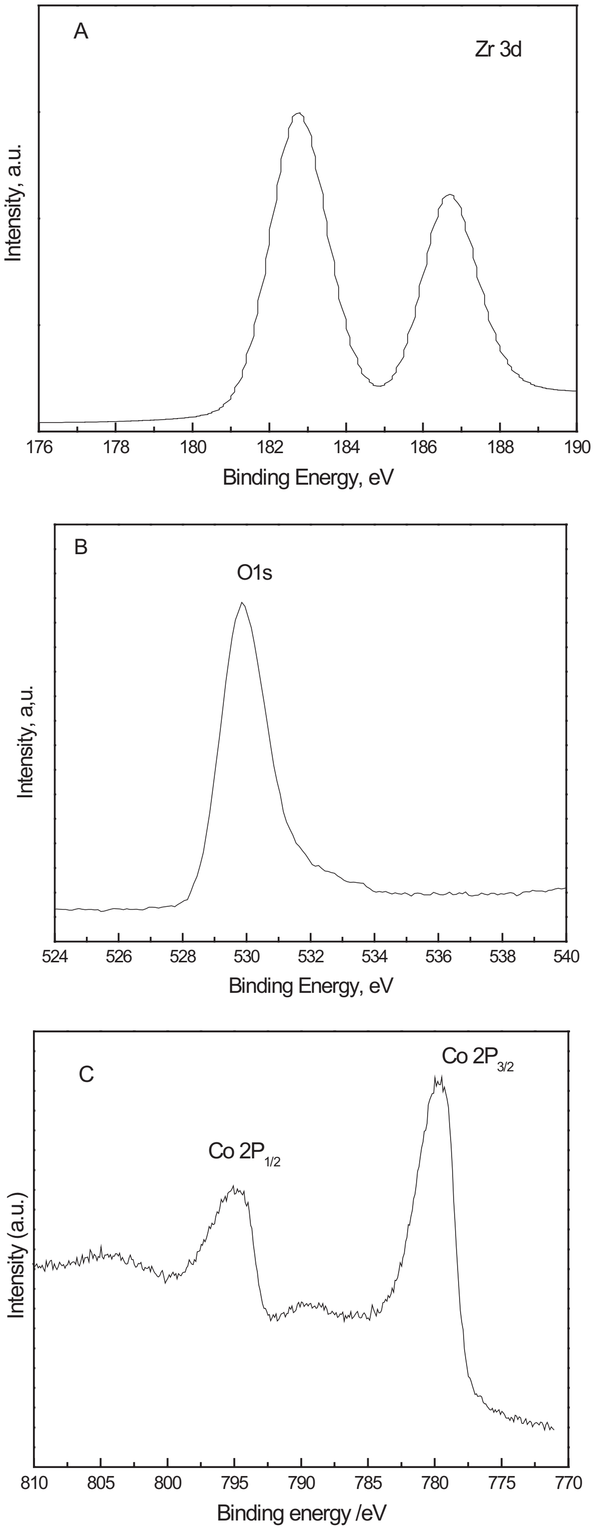

Fig. 2. XPS high-resolution spectra for Zr(A), O(B) and Co(C) species for the 3 wt% Co_3O_4-ZrO_2 nanocomposites.

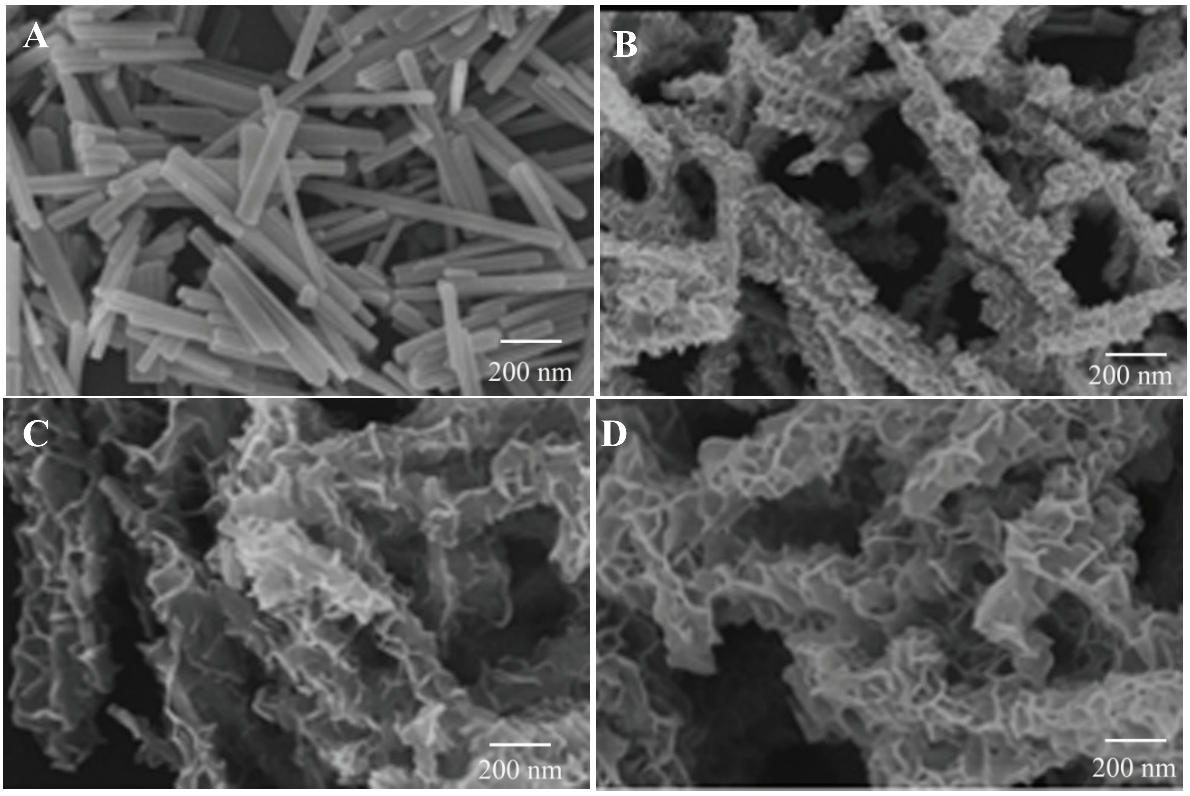

Fig. 3. SEM images of ZrO_2 (A), 1 wt% Co_3O_4-ZrO_2 (B), 3 wt% Co_3O_4-ZrO_2 (C), and 5 wt% Co_3O_4-ZrO_2 (D) samples.

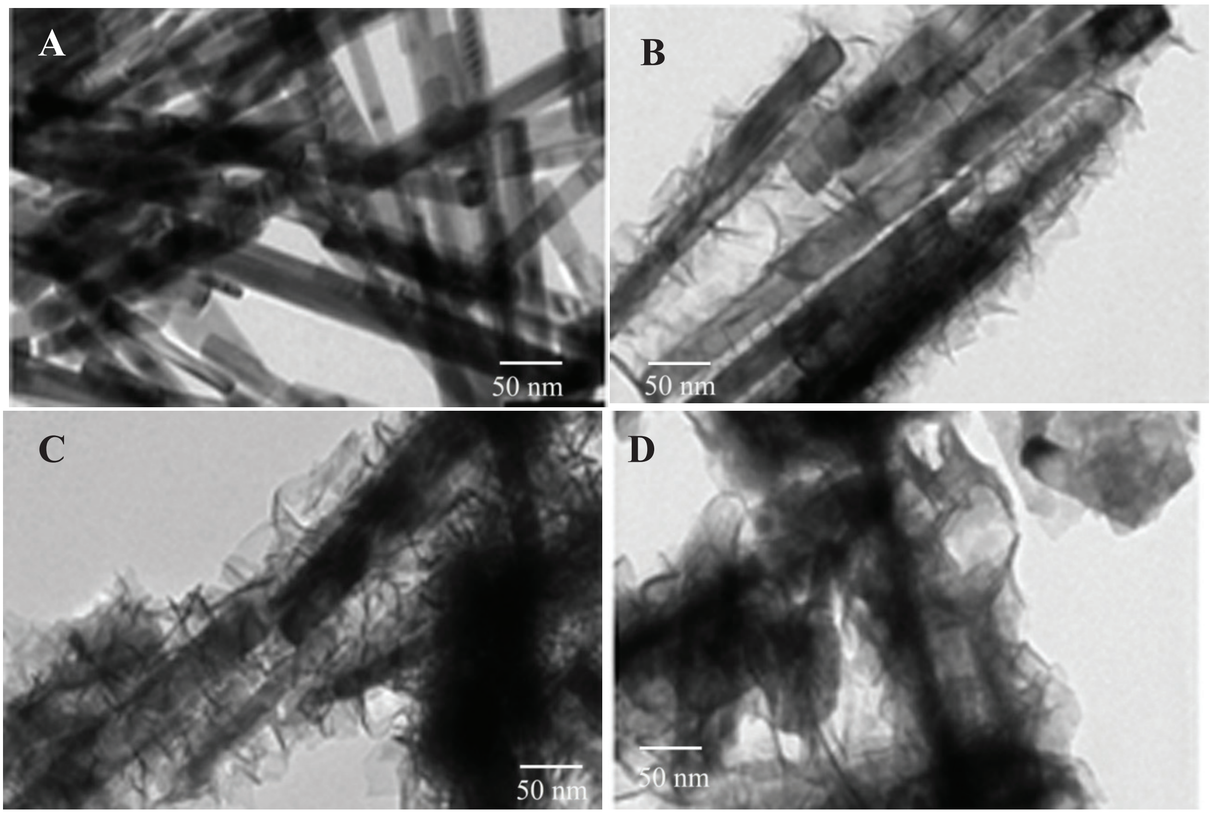

Fig. 4. TEM images of ZrO_2(A), 1 wt% Co_3O_4-ZrO_2 (B), 3 wt% Co_3O_4-ZrO_2 (C), and 5 wt% Co_3O_4-ZrO_2 (D) samples.

cent of Co_3O_4 increased, the percent of nanosheets around the nanorods increased.

Table 1 includes the surface area of the ZrO_2 and Co_3O_4-ZrO_2 nanocomposites. Surface area values of the ZrO_2, 1 wt% Co_3O_4-ZrO_2, 3 wt% Co_3O_4-ZrO_2, and 5 wt% Co_3O_4-ZrO_2% samples are 70.00, 83.50, 89.20 and 89.30 m^2/g, respectively. Additionally, we noted that the incorporation of some of cobalt ions into the zirconium oxide lattice lead to the Co_3O_4-ZrO_2 surface area being higher than that of the ZrO_2 sample. The increase of specific surface area is explained by lattice distortion and it is likely due to the close contact of cobalt oxide nanosheets to zirconia nanorods according to the TEM images. The specific surface area data in text is also inconsistent with Table 1.

Fig. 5A shows the UV-Vis spectra of the ZrO_2 and Co_3O_4-ZrO_2 nanocomposite samples. The results reveal that the addition of Co_3O_4 to ZrO_2 moves the absorption of ZrO_2 from the ultraviolet region to the visible region. An estimate of the optical band gap is obtained using the following equation:

$$\alpha\ (h\gamma) = A\ (h\gamma - Eg)^{m/2}$$

where A is a constant, α is the absorption coefficient, and m equals 1 for a direct transition. The energy intercept of a plot of $(\alpha\ h\gamma)^2$ vs. $(h\gamma)$ yields Eg for a direct transition (Fig. 5B). The band gap values of the ZrO_2, 1 wt% Co_3O_4-ZrO_2, 3 wt% Co_3O_4-ZrO_2, and 5 wt% Co_3O_4-ZrO_2samples are 3.43, 2.80, 2.68 and 2.65 eV, respectively. Therefore, the band gap of ZrO_2 can be adjusted by adjusting the Co_3O_4weight percent. Additionally, controlling the weight percent of Co_3O_4 has an important effect on the photocatalytic activity of ZrO_2, as exhibited in the photocatalytic experiment.

Fig. 6. shows the transient photocurrent responses of the ZrO_2 and 3 wt% Co_3O_4-ZrO_2 samples. The results indicate that the photocurrent density of the 3 wt% Co_3O_4-ZrO_2 sample is higher than that of the ZrO_2 sample. Therefore, the electron-hole recombination rate of ZrO_2 can be adjusted by Co_3O_4 adding. Additionally, the addition of Co_3O_4 to the ZrO_2 sample increases the photocatalytic activity of the ZrO_2 sample, as demonstrated in the photocatalytic activity experiment.

3.2. *Evaluation of photocatalytic activity*

Many parameters affect the photocatalytic activity for the degradation of cyanide, such as the type of photocatalyst, dose of photocatalyst and reuse of the photocatalyst. Fig. 7 shows the effect of Co_3O_4 weight percent on the performance of ZrO_2 for cyanide degradation. The photo

Table 1
BET surface area of ZrO_2 and Co_3O_4-ZrO_2 nanocomposites

Sample	BET surface area, m^2/g
ZrO_2	70.00
1 wt% Co_3O_4-ZrO_2	83.50
3 wt% Co_3O_4-ZrO_2	89.20
5 wt% Co_3O_4-ZrO_2	89.30

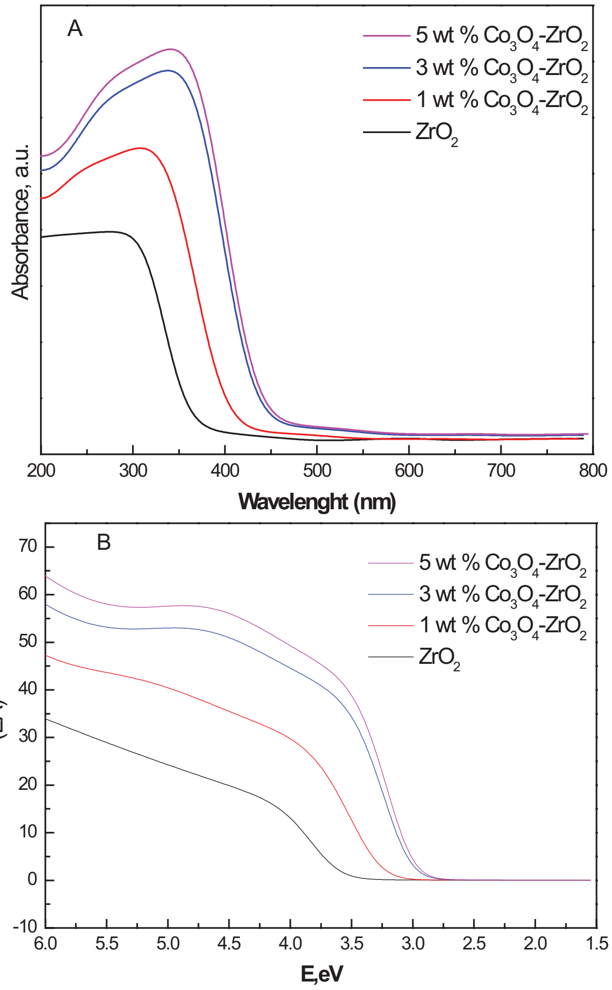

Fig. 5. (A) UV-Vis spectra of the ZrO_2 and Co_3O_4-ZrO_2 nanocomposites samples; (b) plot of transferred Kubelka–Munk versus energy of the light absorbed of pure ZrO_2 and Co_3O_4-ZrO_2 nanocomposites.

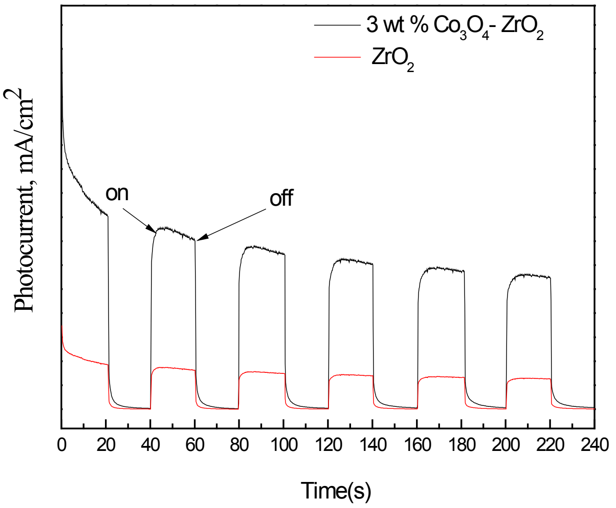

Fig. 6. Transient photocurrent responses of ZrO_2 (A) and 3 wt% Co_3O_4-ZrO_2 (B) samples.

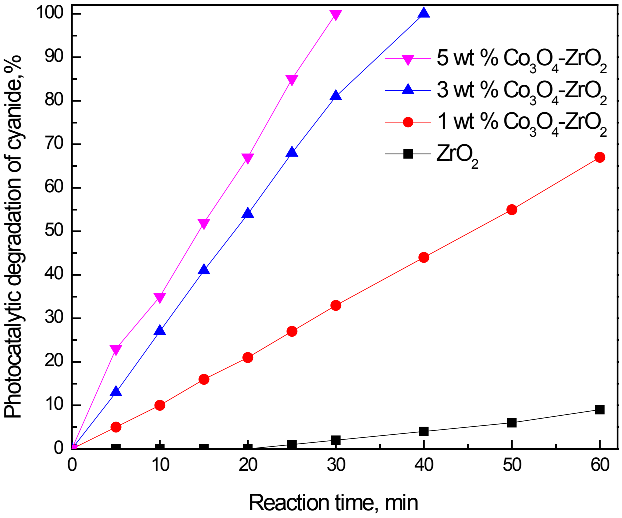

Fig. 7. Effect of the Co_3O_4 weight percent on the performance of ZrO_2 for cyanide degradation.

catalytic experiment was carried out under the following parameters: 100 ppm cyanide concentration, reaction time of 60 min, solution volume of 300 mL, solution pH of 10.5, photocatalyst dose of 1.2 g/L, and visible light irradiation source. The results indicate that the photocatalytic degradation values of cyanide using the ZrO_2 and 1 wt% Co_3O_4-ZrO_2 samples are 9 and 67%, respectively. Because the reaction was carried out under visible light the and ZrO_2 sample absorbs in the ultraviolet region, addition of cobalt oxide to zirconium oxide changed the absorption from the ultraviolet to the visible region. Moreover, we noted that the photocatalytic degradation values of cyanide using the ZrO_2, 1 wt% Co_3O_4-ZrO_2, 3 wt% Co_3O_4-ZrO_2, and 5 wt% Co_3O_4-ZrO_2 samples are 9, 67, 100 and 100%, respectively. This outcome is due to the decreased band gap for ZrO_2, 1 wt% Co_3O_4-ZrO_2, 3 wt% Co_3O_4-ZrO_2, and 5 wt% Co_3O_4-ZrO_2 from 3.43, 2.80, 2.68 and 2.65 eV, respectively. Therefore, the photocatalytic activity of zirconium oxide can be enhanced by increasing the surface area and decreasing the band gap by adding a certain amount of cobalt oxide. The 3 wt% Co_3O_4-ZrO_2 is the optimum sample, at which the photocatalytic activity reached 100% within 40 min.

Fig. 8 shows the effect of the 3 wt% Co_3O_4-ZrO_2 dose on the performance of 3 wt% Co_3O_4-ZrO_2 for cyanide degradation. The photocatalytic reaction was carried out under the following parameters: 100 ppm cyanide concentration, 60 min reaction time, solution volume of 300 mL, solution pH of 10.5, visible light irradiation source and the 3 wt% Co_3O_4-ZrO_2 photocatalyst. The results verified that the cyanide degradation increased from 85 to 100% by increasing the photocatalyst dose from 0.4 to 0.8 g/L. The reaction time, which required complete removal of cyanide, was decreased from 60 to 40 to 30 min by increasing the photocatalyst dose from 0.8 to 1.2 to 1.6 g/L. Additionally, we noted that the increasing the photocatalyst dose from 1.6 to 2.0 to 2.4 g/L decreased the photocatalytic activity from 100% after 30 min to 100% after 60 min and 80% after 60 min, receptively. 1.2 g/L is the optimum photocatalyst dose at which the photocatalytic activity reached 100% within 30 min.

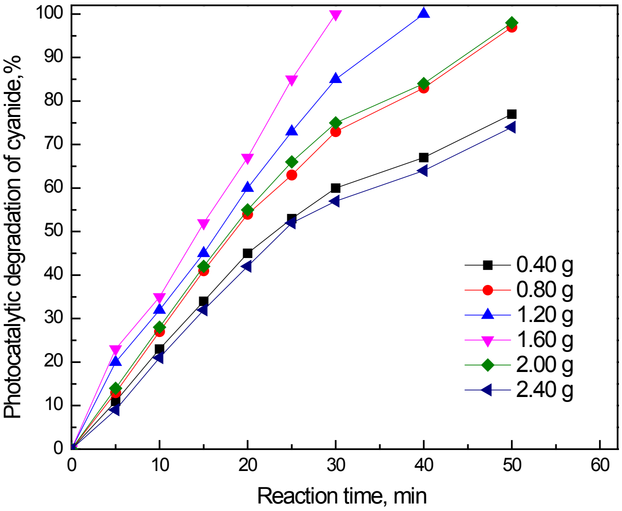

Fig. 8. Effect of 3 wt% Co_3O_4-ZrO_2 dose on the performance of 3 wt% Co_3O_4-ZrO_2 for cyanide degradation.

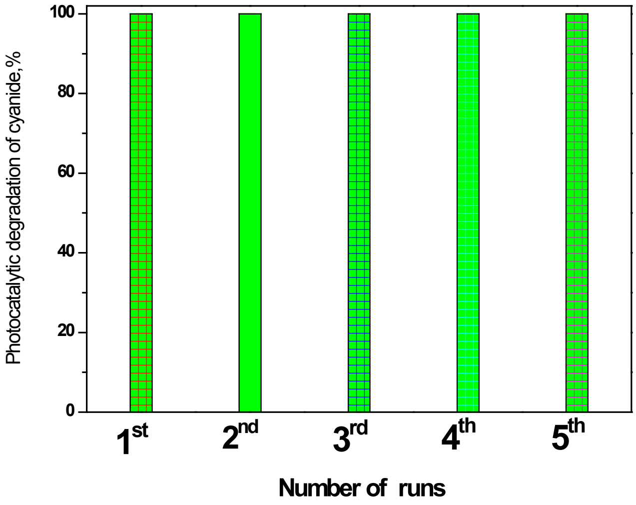

Fig. 9. Effect of reuse 3 wt% Co_3O_4-ZrO_2 photocatalyst on the performance of 3 wt% Co_3O_4-ZrO_2 photocatalyst for cyanide degradation.

Fig. 9 shows the effect of the reuse of the 3 wt% Co_3O_4-ZrO_2 photocatalyst on performance of the 3 wt% Co_3O_4-ZrO_2 photocatalyst for cyanide degradation. The photocatalytic reaction was carried out under the following parameters: 100 ppm cyanide concentration, 30 min reaction time, solution volume of 300 mL, solution pH of 10.5, photocatalyst dose of 1.2 g/L, visible light irradiation source and 3 wt% Co_3O_4-ZrO_2 photocatalyst. The results indicate that the 3 wt% Co_3O_4-ZrO_2 photocatalyst can degrade cyanide many times without decay of its activity.

3.3. Plausible mechanism of Co_3O_4-ZrO_2 photocatalyst

The separation of photogenerated electron and holes between Co_3O_4 and ZrO_2 can be understand by study. The

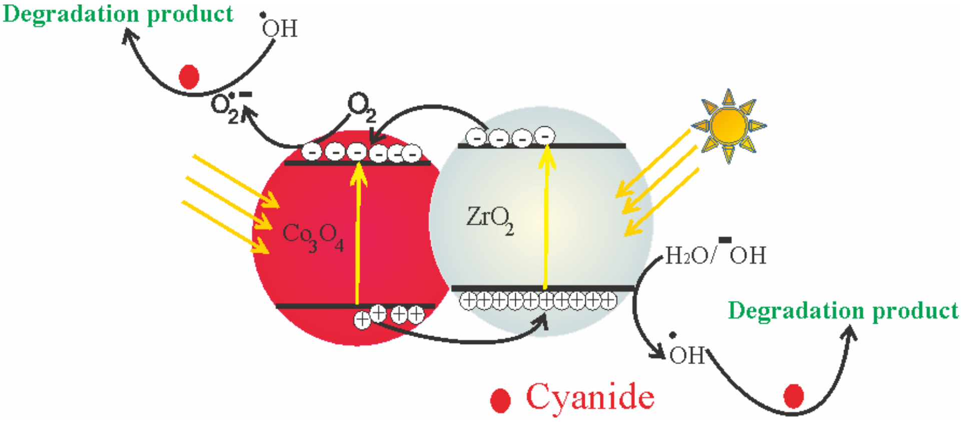

Fig. 10. Schematic diagram of the proposed mechanism for cyanide degradation using Co_3O_4-ZrO_2 photocatalyst.

Table 2
Band gap energies of ZrO_2 and Co_3O_4-ZrO_2samples

Sample	Band gap energy, eV
ZrO_2	3.42
1 wt% Co_3O_4-ZrO_2	2.80
3 wt% Co_3O_4-ZrO_2	2.68
5 wt% Co_3O_4-ZrO_2	2.65

energy level of Co_3O_4 and ZrO_2. The energy level of Co_3O_4 and ZrO_2 can be calculated according to the following experiential formulae:

$$E_{CB} = X - 0.5\,E_g + E_0 \tag{1}$$

$$E_{VB} = E_g + E_{CB} \tag{2}$$

where E_{CB} is conduction band edge and E_{VB} is valence band edge, X is the absolute electronegativity of the semiconductor, E_g is the band gap energy, and E_0 is a measuring scale factor for the redox level of the reference electrode with respect to the absolute vacuum scale (E_0 = –4.5 eV for (NHE) normal hydrogen electrode. Schematic diagram of the proposed mechanism for cyanide degradation of 3 wt% Co_3O_4-ZrO_2 nanocomposite is shown in Fig. 10. As seen from Tables S1, the electrons could be photogenerated from VB of ZrO_2 to its CB. Since the CB level (+0.09) of Co_3O_4 is more positive than the CB level (–0.30) of ZrO_2 in 3 wt% Co_3O_4-ZrO_2, Co_3O_4 can trap the excited electrons from CB of ZrO_2 in 3 wt% Co_3O_4-ZrO_2 as transporter and collector, thus achieving the improved charge separation. Meanwhile, coupling Co_3O_4 with ZrO_2 could also increase the cyanide degradation active sites on the surface of ZrO_2 and accelerate the cyanide degradation kinetics. Therefore, Co_3O_4 coupled with ZrO_2 can simultaneously achieve the accelerated separation of the photogenerated charges, and the improved cyanide degradation kinetics, thus, significantly enhancing the overall photocatalytic efficiency. The superior Co_3O_4 electronic acceptability can greatly promote the photodegradation efficiency.

4. Conclusions

ZrO_2 and Co_3O_4-ZrO_2 nanocomposites were synthesized by a modified sol-gel route. The weight percent of cobalt oxide can control the band gap energy of zirconium dioxide. The band gap of zirconium dioxide was reduced from 3.42 to 2.65 eV by the addition of 3 wt% cobalt oxide. Co_3O_4-ZrO_2 nanocomposites have high photocatalytic activity compared to ZrO_2 due to increased surface area, decreased band gap energy and hindrance of the recombination of electrons and holes. The Co_3O_4-ZrO_2 nanocomposites can degrade 100 ppm of potassium cyanide within 30 min using a 1.2 g/L photocatalyst dose. Co_3O_4-ZrO_2 nanocomposites have photocatalytic stability for five reuses.

Acknowledgments

The authors would like to express their gratitude to King Khalid University, Saudi Arabia for providing administrative and technical support.

References

[1] R.R. Dash, A. Gaur, G. Balomajumder, Cyanide in industrial wastewaters and its removal: a review on biotreatment, J. Hazard. Mater., 163 (2009) 1–11.

[2] R.R. Dash, C. Balomajumder, A. Kumar, Removal of cyanide from water and wastewater using granular activated carbon, Chem. Eng. J., 146 (2009) 408–413.

[3] C. Karunakaran, Semiconductor catalyzed photodetoxification of cyanide, in: S. Kaneco (Ed.), Photo/Electrochemistry & Photobiology in the Environment,Energy and Fuel, Research Signpost, Trivandrum, 2006, pp. 259–294.

[4] J. Marugan, R. van Grieken, A.E. Cassano, O.M. Alfano, Scaling-up of slurry reactors for the photocatalytic oxidation of cyanide with TiO_2 and silica-supported TiO_2 suspensions, Catal. Today, 144 (2009) 87–93.

[5] J. Marugan, R. van Grieken, A.E. Cassano, O.M. Alfano, Intrinsic kinetic modeling with explicit radiation absorption effects of the photocatalytic oxidation of cyanide with TiO_2 and silica-supported TiO_2 suspensions, Appl. Catal. B, 85 (2008) 48–60.

[6] A.A. Ismail, I.A. Ibrahim, M.S. Ahmed, R.M. Mohamed, H. El-Shall, Sol-gel synthesis of titania-silica photocatalyst for cyanide photodegradation, J. Photochem. Photobiol. A, 163 (2004) 445–451.

[7] A. Bozzi, I. Guasaquillo, J. Kiwi, Accelerated removal of cyanide from industrial effluents by supported TiO_2 photocatalysts, Appl. Catal. B, 51 (2004) 203–211.

[8] K. Chiang, R. Amal, T. Tran, Photocatalytic oxidation of cyanide: kinetic and mechanistic studies, J. Mol. Catal. A, 193 (2003) 285–297.

[9] J. Aguado, R. van Grieken, M.J. Lopez-Munoz, J. Marugan, Removal of cyanides in wastewater by supported TiO_2-based photocatalysts, Catal. Today, 75 (2002) 95–102.

[10] R.M. Mohamed, E. Aazam, Effect of Sn loading on the photocatalytic aniline synthesis activity of TiO_2 nanospheres, J. Alloys Compd., 595 (2014) 8–13 .

[11] A.A. Ismail, D.W. Bahnemann, Mesoporous titania photocatalysts: preparation, characterization and reaction mechanisms, J. Mater. Chem., 21 (2011) 11686–11707.

[12] S. Chang, R. Doong, Interband transitions in sol–gel-derived ZrO_2 films under different calcination conditions, Chem. Mater., 19 (2007) 4804–4810.

[13] H. Koohestani, S.K. Sadrnezhaad , Improvement in TiO_2 photocatalytic performance by ZrO_2 nanocompositing and immobilizing , Desal. Water Treat., 57 (2016) 28450–28459.

[14] J. Zhang, Y. Gao, X. Jia, J. Wang, Z. Chen, Y. Xu, Oxygen vacancy-rich mesoporous ZrO_2 with remarkably enhanced visible-light photocatalytic performance, Sol. Energy Mater. Sol. Cells, 182 (2018) 113–120.

[15] J.A. Navio, M.C. Hidalgo, G. Colon, S.G. Botta, M.I. Litter, Preparation and physicochemical properties of ZrO_2 and Fe/ZrO_2 prepared by a sol–gel technique, Langmuir, 17 (2001) 202–210.

[16] K. Kaviyarasu, L. Kotsedi, A. Simo, X. Fuku, T. Mola, J. Kennedy, M. Maaza, Photocatalytic activity of ZrO_2 doped lead dioxide nanocomposites: Investigation of structural and optical microscopy of RhB organic dye, Appl. Surf. Sci., 421 (2017) 234–239.

[17] M. Anpo, T. Nomura, J. Kondo, K. Domen, K.I. Mayura, T. Onishi, Photoluminescence and FT-IR studies of the dissociative adsorption of H_2 on the active ZrO_2 catalyst and its role in the hydrogenation of CO, Res. Chem. Intermed., 13 (1990) 195–202.

[18] S. Chang, R. Doong, The effect of chemical states of dopants on the microstructures and band gaps of metal-doped ZrO_2 thin films at different temperatures, J. Phys. Chem. B, 108 (2004) 18098–18103.

[19] A. Mondal, B. Adhikary, D. Mukherjee, Room-temperature synthesis of air stable cobalt nanoparticles and their use as catalyst for methyl orange dye degradation, Colloids Surf. A Physicochem. Eng. Asp., 482 (2015) 248–257.

[20] J. Almeida, V. Lucia, A. Saraiva, T. Regina, M. Zani, S. Carvalho, Characterization and photocatalytic evaluation of ZnO–Co_3O_4 particles obtained by high energy milling Part II: Photocatalytic properties, Ceram. Int., 42 (2016) 3485–3490.

[21] G. Dai, S. Liu, Y. Liang, T. Luo, Synthesis and enhanced photoelectrocatalytic activity of p-n junction Co_3O_4/TiO_2 nanotube arrays, Appl. Surf. Sci., 264 (2013) 157–161.

[22] Vog. A. I. Vogel, Quantitative Inorganic Analysis, Longmans, London, (1978).

[23] L. He-jian, Z. Li, Z. Tian-qi, X. Xiu-feng, Effect of preparation parameters on the catalytic performance of hydrothermally synthesized Co_3O_4 in the decomposition of N_2O, J. Fuel Chem. Technol., 46(6) (2018) 717–724.

[24] K. Fan, Z. Jin, G. Wang, H. Yang, D. Liu, H. Hu, G. Lu, Y. Bi, Distinctive organized molecular assemble of MoS_2, MOF and Co_3O_4, for efficient dye-sensitized photocatalytic H_2 evolution, Catal. Sci. Technol., 8 (2018) 2352.

[25] C. S. Chua, D. Ansovini, C.J.J. Lee, Y.T. Teng, L.T. Ong, D. Chi, T.S.A. Hor, R. Rajab, Y.-F. Lim, The effect of crystallinity on photocatalytic performance of Co_3O_4 water-splitting cocatalysts, Phys. Chem. Chem. Phys., 18 (2016) 5172.

Supporting materials

Table S1
The electronegativity, band gap, conduction band edge and valance band edge potential of the catalysts on normal hydrogen electrode

Semiconductor	χ ,eV	E_g, eV	E_{CB}, ev	E_{VB}, ev
Co_3O_4	5.93	3.42	+0.09	+ 2.77
ZrO_2	5.91	2.68	–0.30	+3.12

Table S2
Wt % of Co_3O_4 to ZrO_2 as theoretical and as determined by ICP

Sample	Wt % of Co_3O_4 to ZrO_2, calculated	Wt % of Co_3O_4 to ZrO_2, by ICP
1 wt % Co_3O_4-ZrO_2	1: 99	1.0 : 99.0
3 wt % Co_3O_4-ZrO_2	3: 97	2.98 : 97.2
5 wt % Co_3O_4-ZrO_2	5: 95	4.99 : 95.1